Available online at www.sciencedirect.com
SCIENCE DIRECT®
Geochimica et Cosmochimica Acta 70 (2006) 2591–2602
Geochimica
www.elsevier.com/locate/gca

Experimental study of platinum solubility in silicate melt to 14 GPa and 2273 K: Implications for accretion and core formation in Earth

Werner Ertel [a,*], Michael J. Walter [b], Michael J. Drake [c], Paul J. Sylvester [d]

[a] Ludwig Maximilian University, Department of Earth and Environmental Sciences, Theresienstr. 41, D-80333 Munich, Germany
[b] Department of Earth Sciences, University of Bristol, Wills Memorial Building, Queen's Rd., Bristol, BS8 1RJ, UK
[c] Lunar and Planetary Laboratory, University of Arizona, 1629 East University Boulevard, Tucson, AZ, 85721, USA
[d] Department of Earth Sciences, Memorial University of Newfoundland, 300 Prince Philip Drive, St. John's, Newfoundland, Nfld, Canada A1B 3X5

Received 15 September 2004; accepted in revised form 9 February 2006

Abstract

We determined the solubility limit of Pt in molten haplo-basalt (1 atm anorthite-diopside eutectic composition) in piston-cylinder and multi-anvil experiments at pressures between 0.5 and 14 GPa and temperatures from 1698 to 2223 K. Experiments were internally buffered at ~IW + 1. Pt concentrations in quenched-glass samples were measured by laser-ablation inductively coupled-plasma mass spectrometry (LA-ICPMS). This technique allows detection of small-scale heterogeneities in the run products while supplying three-dimensional information about the distribution of Pt in the glass samples. Analytical variations in ^{195}Pt indicate that all experiments contain Pt nanonuggets after quenching. Averages of multiple, time-integrated spot analyses (corresponding to bulk analyses) typically have large standard deviations, and calculated Pt solubilities in silicate melt exhibit no statistically significant covariance with temperature or pressure. In contrast, averages of minimum ^{195}Pt signal levels show less inter-spot variation, and solubility shows significant covariance with pressure and temperature. We interpret these results to mean that nanonuggets are not quench particles, that is, they were not dissolved in the silicate melt, but were part of the equilibrium metal assemblage at run conditions. We assume that the average of minimum measured Pt abundances in multiple probe spots is representative of the actual solubility. The metal/silicate partition coefficients ($D^{met/sil}$) is the inverse of solubility, and we parameterize $D^{met/sil}$ in the data set by multivariate regression. The statistically robust regression shows that increasing both pressure and temperature causes $D^{met/sil}$to decrease, that is, Pt becomes more soluble in silicate melt. $D^{met/sil}$ decreases by less than an order of magnitude at constant temperature from 1 to 14 GPa, whereas isobaric increase in temperature produces a more dramatic effect, with $D^{met/sil}$ decreasing by more than one order of magnitude between 1623 and 2223 K. The Pt abundance in the Earth's mantle requires that $D^{met/sil}$ is ~1000 assuming core-mantle equilibration. Geochemical models for core formation in Earth based on moderately and slightly siderophile elements are generally consistent with equilibrium metal segregation at conditions generally in the range of 20–60 GPa and 2000–4000 K. Model extrapolations to these conditions show that the Pt abundance of the mantle can only be matched if oxygen fugacity is high (~IW) and if Pt mixes ideally in molten iron, both very unlikely conditions. For more realistic values of oxygen fugacity (~IW − 2) and experimentally-based constraints on non-ideal mixing, models show that $D^{met/sil}$ would be several orders of magnitude too high even at the most favorable conditions of pressure and temperature. These results suggest that the mantle Pt budget, and by implication other highly siderophile elements, was added by late addition of a 'late veneer' phase to the accreting proto-Earth.

1. Introduction

The processes of accretion of and core formation in the Earth and other terrestrial planets can potentially be deduced through geochemical modeling. Siderophile, or Fe-loving, elements partition preferentially into Fe-rich planetary cores, making them ideal sensors of core formation. Their chemical distribution between the core and mantle may potentially have recorded the pressure, temperature, redox state, and phase compositions if equilibrium was obtained. Siderophile elements are generally subdivided into

* Corresponding author. Fax: +49 089 2180 4176.
E-mail address: ertel@min.uni-muenchen.de (W. Ertel).

0016-7037/$ - see front matter © 2006 Elsevier Inc. All rights reserved.
doi:10.1016/j.gca.2006.02.015

the moderately siderophile elements (MSE) with metal/silicate partition coefficients ($D^{met/sil}$) $< 10^4$ at 1 atm, and the highly siderophile elements (HSE) with $D^{met/sil} \gg 10^4$ at 1 atm. The HSE include the Pt group elements Ru, Rh, Pd, Os, Ir, and Pt, as well as Re and Au. The abundances of MSE have been used to predict metal-silicate equilibration in Earth at conditions in the approximate range of 20–60 GPa and 2000–4000 K (e.g., Li and Agee, 1996; Righter and Drake, 1997; Gessmann and Rubie, 1998, 2000; Li and Agee, 2001; Chabot and Agee, 2001, 2002, 2003; Wade and Wood, 2005).

The abundances of the HSE in Earth's upper mantle are shown in Fig. 1 (based on data from Newsom, 1990; McDonough and Sun, 1995; Newsom et al., 1996; comp. as well Walter et al., 2000), and exhibit two striking features. First, HSE are measurable in upper mantle samples, which is shocking given their extremely large metal/silicate partition coefficients at 1 atm. For example, Pt, the focus of this study, has a metal/silicate partition coefficient ($D^{met/sil}$) of 7×10^{15} at 1573 K and 1 atm (Ertel et al., 1999), and assuming a redox state of two log units below the iron-wustite buffer (IW − 2). A partition coefficient of this magnitude would strip Pt entirely into a newly forming core, leaving essentially no trace of it in the residual mantle. Second, HSE are present in nearly chondritic relative abundance ratios in the upper mantle. Again this is unexpected based on knowledge of low P–T partitioning experiments, which show large inter-element fractionations (e.g., see review in Walter et al., 2000). These two distinctive features of the HSE have long been interpreted as resulting from a late-addition of oxidized material with chondritic relative abundance levels of the HSE (Kimura et al., 1974; Wänke, 1981; Ringwood, 1984; Wänke et al., 1984; O'Neill, 1991a,b; O'Neill and Palme, 1998; Holzheid and Grove, 2002). The idea is that after core formation ceased, the addition of the 'late veneer' was very efficiently mixed into the mantle, perhaps while in a partially molten state, and that this established the abundances of HSE without significantly perturbing the MSE. This model was challenged by Righter and Drake (1997), who, on the basis of metal/silicate partition coefficients for Re, suggested that like the MSE, metal-silicate equilibrium at conditions of a deep magma ocean could account for the Re abundance in the mantle, obviating the need for a late veneer, at least for this element. To further test this hypothesis, we have investigated the pressure and temperature dependence of the solubility limit of Pt in molten silicate liquid.

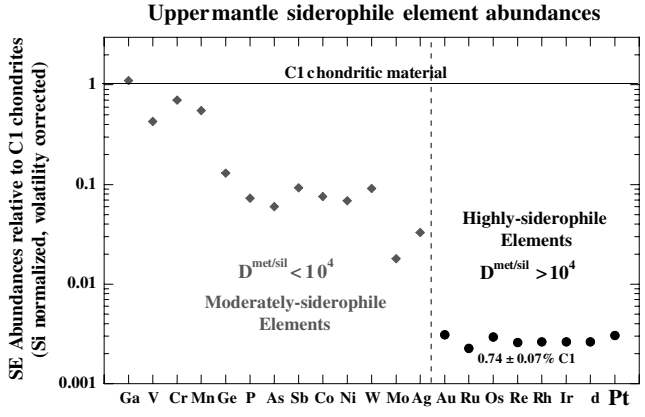

Fig. 1. Upper mantle siderophile element abundances normalized to C1 chondrites and Si (compiled from data of Newsom, 1990; McDonough and Sun, 1995; and Newsom et al., 1996; see as well Walter et al., 2000).

2. Experimental procedures

We performed high-pressure experiments at 0.5, 1, and 2 GPa using a 1/2-inch Holloway Quickpress at the Lunar and Planetary Laboratory (LPL) of the University of Arizona (details below). Experiments at pressures from 4 to 14 GPa were performed at the Institute for Study of the Earth's Interior (Okayama University, Misasa, Japan) using a split-sphere type multi-anvil press. Temperatures were in the range of 1698–2223 K, being ultimately constrained by the melting points of the Pt capsule and the AnDi starting material, as shown in Fig. 2.

The partitioning behavior of Pt as a function of oxygen fugacity and temperature is well studied in the 1 atm anorthite-diopside eutectic composition (AnDi), using both mechanically assisted equilibration techniques (Dingwell et al., 1994; Ertel et al., 1999), and loop techniques (Borisov and Palme, 1997). To eliminate composition as a variable and to facilitate direct comparison of our high

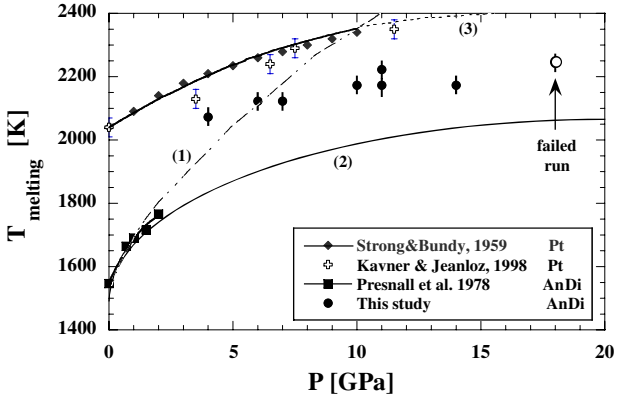

Fig. 2. Plot of melting temperature of AnDi and Pt (°C) vs. pressure (GPa) in MA experiments: melting temperatures of Pt (Strong and Bundy, 1959, filled diamonds; and Kavner and Jeanloz, 1998, open crosses) and AnDi eutectic composition (Presnall et al., 1978; filled squares) in dependence on increasing pressure (GPa). Pt melting point defines the upper experimental limit, while AnDi melting temperature (and extrapolations (1) and (2)) define the minimum temperature limit. All MA experiments (black dots) were entirely molten and define lower limits for MA experiments with AnDi starting material, illustrated by the dotted lines (1) and (2) as extrapolations of the Presnall et al. (1978) data to higher pressures: (1) using the first 3 data points resulting in a steeper increase of AnDi melting point with increasing pressure; (2) using all data points resulting in lower melting points with increasing pressure; (3) extrapolation of the Strong and Bundy (1959) and Kavner and Jeanloz (1998) melting point data of Pt to higher pressures.

pressure results with those determined in 1 atm experiments we also use the 1 atm AnDi eutectic composition in our high-pressure experiments. This composition also has the advantage that it quenches to a homogeneous (i.e., major elements) and crystal free glass.

Powdered glass of AnDi composition was synthesized from reagent grade MgO, $CaCO_3$, Al_2O_3, and SiO_2 by fusion of intimately mixed oxide components in an Al_2O_3 crucible in a muffle furnace at 1673 K for 30 min. AnDi glass was obtained by removing the Al_2O_3 crucible from the muffle furnace and quenching in air. The starting glass was finely ground to a powder using an agate mortar. LA-ICPMS measurements show no detectable Pt concentrations (below 1 ppb) in the starting material. We added about 1 wt% graphite powder to the starting mixture to function as an internal C-CO-CO_2 buffering system (see French and Eugster, 1965; French, 1966; Wendlandt, 1982; Hillgren, 1991). To ensure buffer capacity over long run durations, an additional piece of pure graphite was encapsulated inside the Pt container. The C-CO-CO_2 buffer results in an effective oxygen fugacity about 1 log unit above the IW buffer ($\sim$IW + 1) (French and Eugster, 1965; French, 1966; Wendlandt, 1982; Hillgren, 1991), with a reproducibility of the buffer conditions of at least IW + 1 ± 0.5 (French and Eugster, 1965).

2.1. Piston cylinder experiments

Platinum capsules of 3 mm outer diameter and 6 mm length were packed with the starting glass mixture (about 25–30 mg of AnDi + 1 wt% C) and a small piece of graphite (about 5 wt% of the total weight of the AnDi mixture). Pt capsules were welded shut under Ar, and tested for leaks in a hot paraffin oil bath. The weight of each component (AnDi + 1 wt% C, C-piece, Pt capsule, and cap) and total capsule weight was determined for each run. Total capsule weight was measured before and after each run, and only capsules with unchanged weight are included in the data set.

Experiments at 0.5, 1, and 2 GPa were performed using $BaCO_3$ as a pressure medium (details are given in Righter et al., 1997). Temperature measurement is made directly below the Pt capsule using 0.25 mm W_5Re_{95}-$W_{26}Re_{74}$ thermocouple wire. Run temperatures were held constant to ±2 °C over the entire run duration (1–50 h). Experiments were quenched by shutting off power to the graphite heater, while increasing the cooling water flow. Quench rates were initially larger than 500 °C per second, which was fast enough to quench all experiments to crystal-free, homogeneous glass.

Retrieved Pt capsules were embedded in epoxy and sectioned along the long axis, and were polished to 1 μm finish. We checked glass samples for homogeneity under an optical microscope (40×). No gas bubbles, particles or crystals were observed, but a small melt-free space was present inside each Pt capsule, which we attribute to the presence of a C-containing gas atmosphere formed during quench. Five glass samples (PC-92, 93, 94, 95, and 114) were a slightly brownish color, possibly due to finely precipitated graphite.

Time series experiments establish the time required to achieve a steady-state solubility in experiments at 0.5, 1, and 2 GPa, and temperatures of 1773 and 1823 K (Table 1). Isobaric, isothermal experiments were performed between 1 and 50 h, and results are graphically portrayed in Fig. 3. Steady state concentrations of Pt are established after about 10–12 h for conditions of 1823 K at 2 GPa, and about 12–15 h at 1773 K at 1 GPa. Fig. 3 shows that an increase in temperature of only 50 K results in a reduction of the necessary duration for attainment of equilibrium of Pt from 15 to about 10 h. Both time series exhibit a maximum of the Pt concentration around 1–2 h. This transient maximum is likely due to initial oxidation of Pt by oxygen trapped during capsule welding. Pt is oxidized during welding in air, and dissolves in the melt upon initial heating under relatively oxidizing conditions, resulting in an increase of the Pt concentration. The C-CO-CO_2 buffer system eventually reduces the amount of dissolved Pt according to its oxygen fugacity ($\sim$IW + 1), and in consequence lowers the solubility of Pt to equilibrium values.

To ensure attainment of equilibrium piston-cylinder experiments routinely had run durations of $\sim$10 h or more. Runs performed at temperatures lower than those of time series were run up to 50 h to compensate for slower kinetics, whereas higher temperature runs were sometimes of shorter duration. Conditions for all experiments are provided in Table 1.

2.2. Multi-anvil experiments

Experiments were performed from 4 to 14 GPa, and 2123–2223 K in an 6/8-type multi-anvil press. Cr-doped MgO octahedral pressure cells with 18 and 14 mm edge lengths were compressed within tungsten-carbide cubes with 11 and 8 mm truncations, respectively. Pressures were calibrated using a standard set of fixed-point phase transitions at both room- and high-temperature (Walter et al., 1995). High temperatures were achieved using either graphite (18/11 cell) or Re (14/8 cell) heaters, and temperatures were monitored with W_5Re_{95}-$W_{26}Re_{74}$ thermocouples. A temperature gradient of less than 50 K around the hot spot is assumed based on previous experience with similar cell designs. Run temperatures were held constant to within ±2 K. Samples were quenched by switching off the power.

Pt capsules were prepared as described above for piston-cylinder experiments, except that the Pt tube was about 1.5 mm in diameter and 4 mm in length, and contained approximately 2 mg of AnDi-C starting mixture and a graphite piece of $\sim$0.5 mg. Performance of time series runs as described in PC experiments were not possible as experiments using Re heaters, had a tendency to fail shortly after 1 h of total run duration at the highest temperatures. However, based on the much smaller capsule size and the amount of melt (which is of the order of 1/12 of a standard PC run), and faster diffusion at higher run temperatures

Table 1
Experimental conditions and analytical results for Pt concentration (ppb) in silicate melt from LA-ICPMS

Experimental conditions				Bulk (ppb)[a]						Average-lowest (ppb)[b]							Minimum[c] (ppb)
Run#	P (GPa)	T (K)	t (h)	#1/#5[d]	#2/#6	#3/#7	#4/#8	Ave.	SD	#1/#5	#2/#6	#3/#7	#4/#8	N[e]	Ave.	SD	
PC-129	0.5	1773	24	2271	396	647	1170	1121	720	365	181	292	220	4	265	81	181
PC-130[f]	0.5	1773	12	4794	2130	3462	1688	3019	1215	677	673	722	690	4	691	22	673
PC-131[f]	0.5	1773	6	2248	6088	4576	7814	5182	2045	419	1237	2838	1892	4	1597	1023	419
PC-132[f]	0.5	1773	3	8536	5441	5425		6467	1463	1392	2199	1322		3	1638	487	1322
PC-134	0.5	1823	12	436	516	554		502	49	331	370	402		3	368	36	331
PC-135[f]	0.5	1773	2	20326	10279	15470	15045	15280	3555	6345	4408	6064	4647	4	5366	980	4408
PC-137[f]	0.5	1773	1	9992	14964	6401	10691	10512	3042	1933	2031	2906	2827	4	2424	513	1933
PC-138	0.5	1873	12	275	235	240		250	18	146	114	96		3	119	25	96
PC-140[f]	0.5	1773	3	20017	69343	22693		37351	22648	559	12700	6188	4622	3	3790	2905	559
PC-144	0.5	1923	2	1317	823	1409		1183	257	569	488	634		3	564	73	488
PC-145	0.5	1723	50	17403	10615	2612	2877			3596	3308	371	158				
cont.				1396				6981	6147	287				3	272	88	158
PC-151[f]	0.5	1773	3	5949	15011	8007	8307	9319	3410	1773	2122	2432	2435	4	2191	315	1773
PC-157	0.5	1723	50	8328	19315	23225	3267	13534	8060	113	385	655	282	3	260	137	113
PC-159[f]	0.5	1723	8.5	8717	2432	1968	3961			1818	348	416	627				
cont.				41536				11723	15097	1025				4	604	304	348
PC-88[f]	1	1773	10	3023	4823	2510	5366	3931	1194	446	863	383	734	4	607	229	383
PC-89[f]	1	1773	6.2	8941	3797	3637	7527			578	806	759	1112	4			
cont.				24022	5577	12690		9456	6628	2053	544	2076			671	130	544
PC-91	1	1823	9	264	224	322	266	269	35	247	219	209	245	4	230	19	209
PC-92	1	1873	10	188	421	658	537	451	173	173	211	174	288	4	212	54	173
PC-93	1	1923	9	687	638	783	662	693	55	621	613	710	595	4	635	51	595
PC-94	1	1973	9	753	2830	679	756	1255	910	716	846	676	721	4	740	74	676
PC-95	1	1723	25	138	1350	149	188	456	516	118	376	135	129	3	127	7	118
PC-96	1	1698	29	708	2976	89583	601	23467	38184	43	180	831	34	3	86	67	34
PC-97[f]	1	2023	3	1087	1188	1369		1215	117	358	543	724		3	542	183	358
PC-98	1	2023	4.8	1715	2044	1238		1666	331	848	768	814		3	810	40	768
PC-102	1	1773	48	2485	912	1976		1791	655	118	215	402		3	245	144	118
PC-103[f]	1	1773	20	1828	807	328	1336	1075	562	91	139	118	114	4	116	20	91
PC-104[f]	1	1773	26	675	1354	477	366	718	384	139	83	111	144	4	119	28	83
PC-105[f]	1	1773	3	5523	5284	6070	8101	6245	1109	1659	1865	1860	1911	4	1824	112	1659
PC-106[f]	1	1773	2	2409	1139	10177		4575	3995	357	239	1564		3	720	733	239
PC-107[f]	1	1773	1	25188	71204	17565	14760	32179	22852	11435	6995	9359	5053	4	8211	2779	5053
PC-113	1	1723	36	208	193	186		196	9	150	152	190		3	164	23	150
PC-114	1	1723	50	226	86	235	199			45	30	38	24				
cont.				2043	214	1821	423	656	744	47	28	581	532	6	35	9	24
PC-115[f]	2	1823	7	1297	741	757		932	258	642	680	683		3	668	23	642
PC-116[f]	2	1823	25	2649	2592	2768		2670	73	598	636	626		3	620	20	598
Pc-117	2	1823	50	989	1384	1379		1251	185	332	432	371		3	378	50	332
PC-118[f]	2	1823	4.5	4971	4852	4209	2879	4228	831	1203	1179	1214		3	1199	18	1179
PC-119[f]	2	1823	12	899	1121	933		984	98	320	365	281		3	322	42	281
PC-121[f]	2	1823	2	3695	2637	3442	2618	3098	479	886	743	742	792	4	791	68	742
PC-122	2	1873	12	1445	992	1002		1146	211	656	599	687		3	647	45	599
PC-123	2	1923	12	1288	525	3618	4066			1191	508	2788	2616				
cont.	2			3046				2509	1369	1748				3	1149	507	508
PC-124[f]	2	1973	12	392	410	362		388	20	255	277	249		3	260	15	249
PC-125[f]	2	1823	1	1321	1086	1046		1151	121	898	1087	1057		3	1014	102	898
PC-126	2	1773	48	952	584	769		768	150	899	621	795		3	772	140	621
PC-127	2	2023	2	1694	1811	1626		1710	76	1392	1636	1776	1439	4	1561	128	1392
PC-128	2	2023	12	12227	2688	3343		6086	4351	1627	1588	1676		3	1630	44	1588
MA-1	4	2073	1	4728	2966	3587		3760	730	4239	2776	3627		3	3547	735	2776
MA-5	6	2123	1	7782	7231	4401		6471	1481	5379	6541	3529		3	5150	1519	3529
MA-2	7	2123	1	6777	7765	6965		7169	428	2883	4126	4137		3	3715	721	2883
MA-10	10	2173	1	38603	300175	264960		201246	115901	5793	150443	32945		1	5793		5793
MA-6	11	2223	1	51842	58190	705288		271773	306552	17050	23818	204542		2	20434	3384	17050
MA-3	11	2173	1	9295	11337	13323		11318	1645	9143	10401	12057		3	10534	462	9143
MA-9	14	2173	1	34461	25553	9393		23136	10376	3134	3858	2354		3	3115	752	2354
MA-11	14	2173	1.25	7577	3861	5684		5707	1517	7033	3971	5822		3	5609	1542	3971

[a] Bulk, average of entire ablation signal intensities of all spot analyses on single sample.
[b] Average-lowest, average of minimum signal intensities observed in multiple spots on single sample.
[c] Absolute minimum signal intensity observed on a single sample in all analyses.
[d] Spot #. In the case of more than 4 spots, #1/#5 refers to spot 1 or 5, respectively.
[e] Number N of analyses included in the average of "average-lowest" observed values.
[f] PC time series experiment.

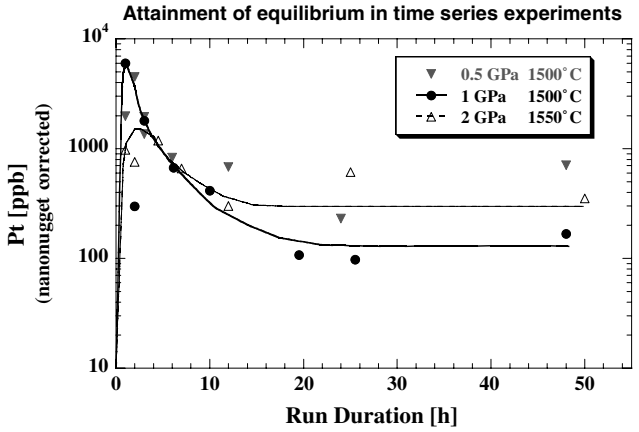

Fig. 3. Time series results at 0.5, 1, and 2 GPa and at 1500 °C or 1550 °C. Solubility of Pt (ppb) is plotted vs. run duration (h) of experiment (see Table 1). Run durations of 10–12 h depending on temperature are sufficient to obtain steady-state Pt abundances in AnDi eutectic melt composition over sample dimensions (5 mm length, 3 mm diameter prior to experimental use).

(2123–2223 K in MA vs. 1723–1973 K in PC runs), we assume that equilibrium solubilities were obtained within an hour. Conditions for all experiments are provided in Table 1.

3. Analytical procedures

3.1. Major element composition—electron microprobe analyses

Major element compositions of the quenched glass samples were determined using a CAMECA SX 50 electron microprobe at the University of Arizona. Operating conditions were a 15 kV accelerating voltage, 20 nA sample current on brass, 20 s counting times, a point beam of approximately 1 μm, and a PAP correction procedure (Pouchou and Pichoir, 1984). Standards were anorthite (Al, Ca) and diopside (Mg, Si). For determination of major elemental composition and to check for heterogeneity in the glass composition, line scans of fifty data points were made over the entire sample length (~1–2 mm). No systematic heterogeneity was detected. The graphite content of the glasses was not determined due to the presence of a graphite coating during sample preparation. The average major element glass composition corresponded to the 1 atm anorthite–diopside eutectic composition (MgO: 10.8%; Al_2O_3: 15.8%; CaO: 23.5%; SiO_2: 49.9%) within analytical uncertainty.

3.2. Trace element composition—laser-ablation inductively coupled-plasma mass spectrometry analyses

The solubilities of HSE like Pt are extremely low in silicate melts even under oxidizing conditions, which has been a major obstacle in previous HSE experimental investigations. The advent of laser-ablation inductively-coupled plasma mass spectrometry (LA-ICPMS) as a routine method for analyzing low concentrations of HSE has largely removed this limitation. LA-ICPMS offers the advantage of sufficiently low detection limits for HSE (e.g., Pt = 500 ppt; Re = 2 ppb) to permit the precise analyses necessary. Performing analyses in the time-resolved acquisition mode provides three-dimensional information about the trace element distribution within the sample, down to the resolution of a single laser pulse. This capability is essential because of the nanonugget formation problem, discussed in detail below and previously (Ertel, 1996; Ertel et al., 1999, 2001; Borisov and Palme, 1994,a,b,c; 1995, 1998).

Platinum concentrations were determined using a Fisons Plasma Quad PQ2+-S ICP-MS instrument at Memorial University of Newfoundland. Platinum analyses were performed as described by Sylvester and Eggins (1997). A 70 μm laser-beam created by a 1064 nm Nd-YAG-laser, quadrupled to a wavelength of 266 nm for better coupling with the silicate glass, gave very reproducible ablation. The laser was focused 150 μm above the sample surface through microscope optics. Laser power was 0.1 J/pulse at a repetition rate of 10 Hz, conditions that resulted in ablation pits with sharp rims and no loss of energy due to crack formation. Ablated material was flushed by a He–Ar gas mixture into the ICP-part of the mass spectrometer at 0.85–0.91 l He/min (cell gas) and 0.5–0.8 l Ar/min. ^{195}Pt and ^{194}Pt isotopes were measured, with ^{187}Re and ^{178}Hf as quality checks of ablation. A 1 atm AnDi eutectic composition standard glass containing 1 ppm Pt (1.055 ± 0.020 ppm, as determined by solution ICPMS with external calibration against a synthetic standard solution of Pt) was prepared in 1 atm stirred Pt crucible experiments (Ertel, 1996; Ertel et al., 1999) for use as a standard. Since the physical and chemical properties of sample and standard matrices are identical, differences in ablation between standard and sample are a function only of laser power fluctuations, not differences in laser-sample coupling. ^{44}Ca and ^{28}Si were used as internal standards to correct for variations in ablation yields and instrument sensitivities over the course of each analysis.

All measurements were performed in a time-resolved working mode. Each measurement started with a minimum of at least 40 to 60 s counting of the background, with the laser beam blocked from the sample by the power meter, which was used to determine absolute laser power and stability over the entire analytical session. Almost no counts on ^{194}Pt and ^{195}Pt were detected, resulting in a very low detection limit of 500 ppt Pt.

During a typical sample measurement, a spot near the centre of a sample was selected, the power meter was removed from the laser beam path, and ablation of glass was initiated. An immediate increase of the signal up to 10^6–10^8 counts/s was observed in the samples with highest Pt concentrations. Time-resolved ablation spectra were collected on a minimum of three spots per sample. If spectra showed significant intensity variability, presumably due to nanonuggets, up to 8 measurements were acquired.

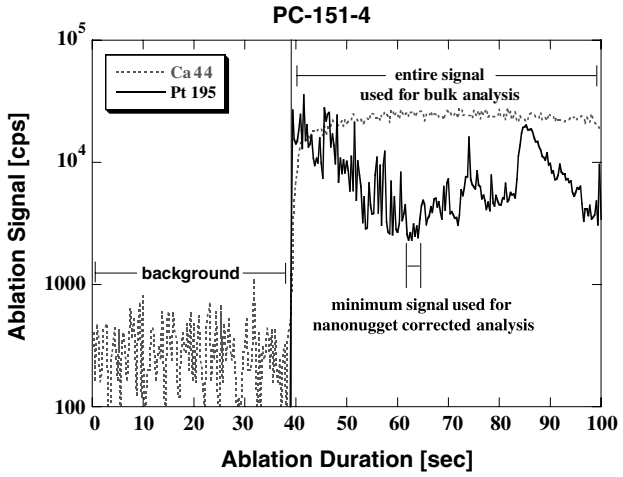

Fig. 4. Representative example of a time resolved ablation spectrum (sample PC-151-4). Signal intensities of ^{44}Ca (grey dashed line) and ^{195}Pt (black solid line) in raw counts (counts/sec) are plotted vs. ablation duration (s). After approx. 40 s without ablation (^{44}Ca signal of "background"; no ^{195}Pt signal), laser is focused on sample surface and ablation is initiated ("signal"). The ^{195}Pt signal immediately increases while ablation takes place. Nanonugget influence is visible in broad 'hills,' 'spikes,' and noise in general in the ablation signal. A "bulk" spot analysis is obtained if the entire signal is used for integration and concentration determination. For nanonugget corrected analyses (="average-lowest" in Table 1 and 2), the minimum signal intensity observed for the spot is used as indicated.

Raw counts were converted into elemental concentrations using the LAMTRACE program at Memorial University (written by S.E. Jackson; see Van Achterbergh et al., 2001). Fig. 4 shows ^{195}Pt counts in a time series run at 1 GPa and 1773 K. The ^{195}Pt signal is highly variable and at relatively high frequency when compared to the ^{44}Ca standard. We attribute this 'spikiness' in the data to the presence of nanonuggets of pure Pt metal within the silicate, the presence of which presents special problems for assessing the Pt abundance as discussed below.

4. Results

4.1. Nanonuggets and LA-ICPMS data treatment

Nanonuggets are a fundamental problem in experimental investigations of HSE partitioning, and are thought to be responsible for the increasing scatter in solubility data at very low oxygen fugacity conditions. Unfortunately, in spite of tremendous experimental effort, little is known about their formation, chemical composition, structure, or size distribution. The primary issue is whether the Pt nanonuggets represent originally dissolved material that emerged upon quench, as suggested by Cottrell and Walker (2002), or whether they are dispersed metal fragments that are part of the equilibrium metal assemblage. If they are originally dissolved material, then the average of numerous, time-integrated spot analyses should be sufficient to accurately reproduce the bulk Pt composition of the silicate. However, if nanonuggets are part of the metal assemblage, then a method must be used to mitigate against corruption of the actual silicate Pt concentration. Clearly, nanonugget pollution of the LA-ICPMS signal will always require a downward correction to measured abundances.

Borisov and Palme (1995) reported the puzzling observation that in a set of Ir-containing samples analysed by INAA, Ir concentrations declined as smaller and smaller sample chips were analysed. The same behavior was observed for Pt, Rh, Re, and Ir by Ertel (1996), Ertel et al. (1999, 2001), and O'Neill et al. (1995) when INAA measurements were duplicated by LA-ICPMS. This observation is now understood to result from nanonuggets as detected by direct spot-analytical measurements of elemental concentrations in silicate glasses using LA-ICPMS. Nanonuggets are heterogeneously distributed as indicated in Fig. 4, possibly due to distinctly different particle sizes and/or populations. Broad 'hills' in ablation spectra presumably represent a relatively homogeneous distribution of smaller nanonuggets of approximately similar size. Abrupt spikes in the spectra are due either to orders of magnitude larger nuggets, or concentrations of smaller nanonuggets. Replicate analyses in a single sample show that each spot has a different time-resolved concentration distribution with variation in the frequency and magnitude of hills and spikes in raw counts. Nanonuggets are, as far as we can observe, heterogeneously distributed throughout the entire sample. From these observations alone, it cannot be deduced whether nanonuggets are formed during quench, as suggested previously by Cottrell and Walker (2002), or are a disseminated part of the metal phase.

Nanonuggets are especially apparent at very low oxygen fugacity conditions in 1 atm experiments containing Ir, Pt, Rh and Re (Borisov and Palme, 1995; Ertel, 1996; Ertel et al., 1999, 2001). Ertel (1996) demonstrated that when using bulk analytical techniques like INAA the concentration of nanonuggets increases with decreasing oxygen fugacity, resulting in an apparent increase in HSE solubility. Such behavior would imply that HSE behave as anions under reducing conditions, an absurd conclusion. LA-ICPMS measurements performed on silicate from the identical samples, however, confirmed the oxygen fugacity dependence of HSE at much more oxidizing conditions. Ertel (1996) reported an apparent increase in nanonugget formation at increasingly reducing conditions when Pt was analysed using INAA, resulting in a strong increase of the observed solubility of Pt, a result similar to that observed by Cottrell and Walker (2002). Ertel (1996) and Ertel et al. (1999) demonstrated at 1 atm that the apparent Pt equilibrium solubilities could be effectively reduced by applying stirred Pt crucible techniques simulating convection over extended periods of time (hundreds of hours), which had the effect of stirring out nanonuggets to form a homogeneous glass, presumably by giving them opportunity to attach to the large metal reservoir. In contrast, static loop experiments at comparable experimental conditions (Borisov and Palme, 1994a,b,c; 1995, 1997; Borisov et al., 1999) resulted in orders of magnitude higher equilibrium

solubilities of HSE compared to stirred Pt crucible experiments, especially under very reduced conditions where nanonuggets dominate the measured elemental solubilities. Experimental observations for four HSE (Pt, Rh, Re, and Ir) indicate that nanonuggets are not dissolved species in the silicate liquid at equilibrium conditions but represent a thermodynamically stable portion of the metal phase (Ertel, 1996; Ertel et al., 1999, 2001).

Nanonuggets are also found in natural samples from the Merensky reef (Ballhaus and Sylvester, 2000). LA-ICPMS analyses of various meteorite samples (Dar al Ghani, Murchison, Allende, Parnallee) showed a heterogeneous distribution of some HSE. Both single-element (Re) and multi-element nanonuggets were identified (Ertel, unpublished data). These observations support our conclusion that nanonuggets are not an artifact of quenching, but form at very reducing conditions in both experiments and nature.

Here we have used three approaches for determining the Pt abundance in the silicate glass based on the LA-ICPMS analyses. The first is to average all time-resolved spot analysis on a given sample. This 'bulk' analysis should give the actual solubility if the nanonuggets are part of the silicate and formed on quench. Two approaches are used to render 'nanonugget-corrected' abundances. We calculate an 'average-lowest' abundance by averaging the minimum abundances (see minimum signal in Fig. 4 for example) observed in up to six separate spots on a sample (typically 4 spots). We also report the absolute minimum Pt abundance (i.e., minimum signal) obtained in any given sample. All analytical data and averages are provided in Tables 1 and 2.

Fig. 5 shows measured Pt abundances in experiments performed at 1 GPa using these different approaches. The data show that bulk averaging produces larger overall standard deviations for each sample (Table 1), relatively large scatter and an ill-defined effect of temperature on solubility. Average-lowest and absolute minimum concentrations yield mutually consistent results and show considerably less statistical variation and a clear trend with temperature. On the basis of these observations and previous experimental results on other HSE, we conclude that the activity of a Pt nanonuggets in the silicate melt corresponds to the activity of the Pt used as container material and source of Pt in

Table 2
Pt solubility limits and metal/silicate partition coefficients

Run#	*P* (GPa)	*T* (K)	Bulk (ppb)[a]			Average-lowest (ppb)[b]			Minimum[c]	
			Ave.	SD	Log D^4	Ave.	SD	Log D^4	(ppb)	Log D^d
PC-145	0.5	1723	6981	6147	5.16	272	88	6.57	158	6.80
PC-157	0.5	1723	13534	8060	4.87	260	137	6.59	113	6.95
PC-129	0.5	1773	1121	720	5.95	265	81	6.58	181	6.74
PC-134	0.5	1823	502	49	6.30	368	36	6.43	331	6.48
PC-138	0.5	1873	250	18	6.60	119	25	6.92	96	7.02
PC-144	0.5	1923	1183	257	5.93	564	73	6.25	488	6.31
PC-96	1	1698	23467	38184	4.63	86	67	7.07	34	7.47
PC-95	1	1723	456	516	6.34	127	7	6.90	118	6.93
PC-113	1	1723	196	9	6.71	164	23	6.79	150	6.82
PC-114	1	1723	656	744	6.18	35	9	7.46	24	7.62
PC-102	1	1773	1791	655	5.75	245	144	6.61	118	6.93
PC-91	1	1823	269	35	6.57	230	19	6.64	209	6.68
PC-92	1	1873	451	173	6.35	212	54	6.67	173	6.76
PC-93	1	1923	693	55	6.16	635	51	6.20	595	6.23
PC-94	1	1973	1255	910	5.90	740	74	6.13	676	6.17
PC-98	1	2023	1666	331	5.78	810	40	6.09	768	6.11
PC-126	2	1773	768	150	6.11	772	140	6.11	621	6.21
PC-117	2	1823	1251	185	5.90	378	50	6.42	332	6.48
PC-122	2	1873	1146	211	5.94	647	45	6.19	599	6.22
PC-123	2	1923	2509	1369	5.60	1149	507	5.94	508	6.29
PC-127	2	2023	1710	76	5.77	1561	128	5.81	1392	5.86
PC-128	2	2023	6086	4351	5.22	1630	44	5.79	1588	5.80
MA-1	4	2073	3760	730	5.42	3547	735	5.45	2776	5.56
MA-5	6	2123	6471	1481	5.19	5150	1519	5.29	3529	5.45
MA-2	7	2123	7169	428	5.14	3715	721	5.43	2883	5.54
MA-10	10	2173	201246	115901	3.70	5793		5.24	5793	5.24
MA-6	11	2223	271773	306552	3.57	20434	3384	4.69	17050	4.77
MA-3	11	2173	11318	1645	4.95	10534	462	4.98	9143	5.04
MA-9	14	2173	23136	10376	4.64	3115	752	5.51	2354	5.63
MA-11	14	2173	5707	1517	5.24	5609	1542	5.25	3971	5.40

[a] Bulk = average of entire ablation signal intensities of all spot analyses on single sample.
[b] Average-lowest = average of minimum signal intensities observed in multiple spots on single sample.
[c] Absolute minimum signal intensity observed on a single sample in all analyses.
[d] Metal/silicate partition coefficient, $D^{met/sil}$, calculated as inverse of solubility (see text).

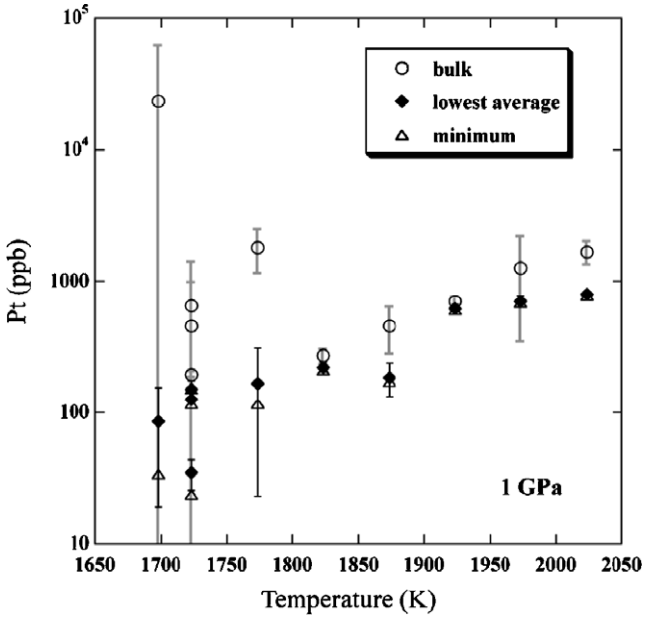

Fig. 5. Pt abundance (ppb) as a function of temperature (K) in experiments made at 1 GPa. Abundances are calculated based on "bulk" averages (open circles), "average-lowest" (solid diamond) and absolute minimum signals (open triangle) as defined in the text and supplied in Table 1.

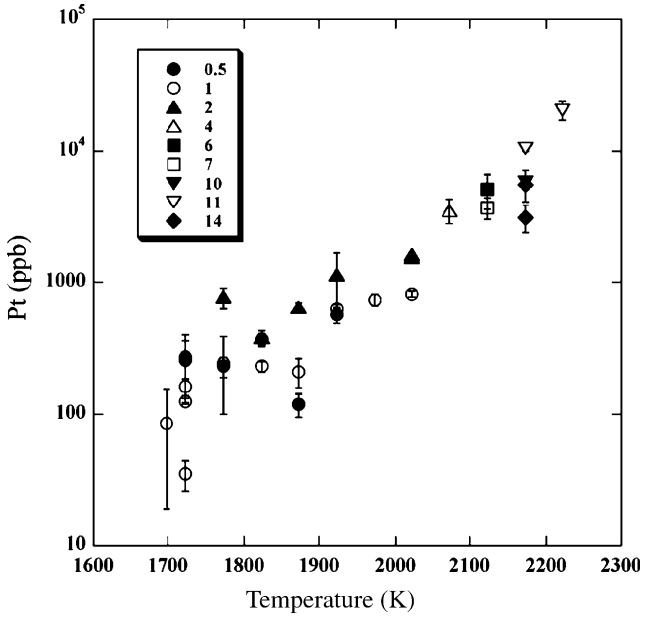

Fig. 6. Experimental Pt solubility limits (ppb) in An-Di eutectic melt as a function of pressure and temperature (between 0.5 and 14 GPa and 1700 and 2223 K, respectively), based on "Lowest-average" Pt abundances as supplied in Table 1.

the experiments. We presume that abundances based on average-lowest data yield reasonably accurate Pt solubilities.

4.2. Temperature and pressure dependence of platinum solubility

Fig. 6 shows Pt solubility in An-Di eutectic liquid at high pressures and temperatures as determined from LA-ICPMS using average-lowest Pt concentrations. Although it is difficult to visually deduce an effect of pressure, there is a distinct increase in solubility with increase in temperature. In order to more strictly define the effects of pressure and temperature we use multivariate least-squares regression. However, rather than using Pt solubility, we prefer to model the data set in terms of the metal/silicate partition coefficient, $D^{met/sil}$, as this is more useful for modeling core formation as presented below. $D^{met/sil}$ represents the weight fraction of Pt in the metal phase to that in the silicate

$$D^{met/sil} = X^{met}/X^{sil}, \quad (1)$$

$D^{met/sil}$ is the inverse of the Pt solubility limit in the silicate in the case of pure metallic Pt, and these values are given in Table 2. Below we discuss the more complicated case of calculating $D^{met/sil}$ for Pt at infinite dilution in metallic iron. In order to quantify and de-convolve pressure and temperature effects on $D^{met/sil}$, we have fitted the entire high-pressure data set to a single multivariate equation of the form:

$$\log D^{met/sil} = \alpha + \beta(1/T) + \chi(P/T), \quad (2)$$

where T is in K and P is in GPa. The advantage of this equation is that it has a general thermodynamic form (Righter and Drake, 1997). Potential disadvantages include interdependence of variables and the inability to reproduce non-linear effects in pressure. Although commonly done and emulated below, extrapolations beyond the range of the fitted data must always be viewed with caution. Table 3 shows regression results for all three methods of analysis (bulk, average-lowest, minimum). The bulk data produce a very poor fit ($R^2 = 0.45$). In contrast, the two nanonugget-corrected methods yield very good fits with $R^2 > 0.8$.

The regressions to the average-lowest data show that both temperature and pressure make Pt more lithophile (increase its solubility), as illustrated in Fig. 7. In general, a 100 K increase in temperature reduces $D^{met/sil}$ by about the same amount as a 4 GPa increase in pressure. Fortenfant et al. (2003) found a similar temperature dependence of the Pt solubility based on 1 atm experiments between 1573 and 1823 K (Fig. 7). However, an impressive discrepancy between 1 atm solubility studies (Ertel et al., 1999; Fortenfant et al., 2003) and our new high-pressure data is a nearly 3 orders of magnitude lower Pt solubility at a

Table 3
Coefficients and statistics for multivariate regressions of the high P–T data to the equation: $\log D^{met/sil} = \alpha + \beta(1/T) + \chi(P/T)$

Fitted data	α	β	χ	R^2
$n = 30$				
Bulk	4.5 (2.0)	2743 (3621)	−236 (85)	0.52
Average-lowest	0.3 (9)	11345 (1740)	−71.5 (40)	0.85
Minimum	0.1 (1.1)	11906 (2063)	−57.1 (49)	0.81

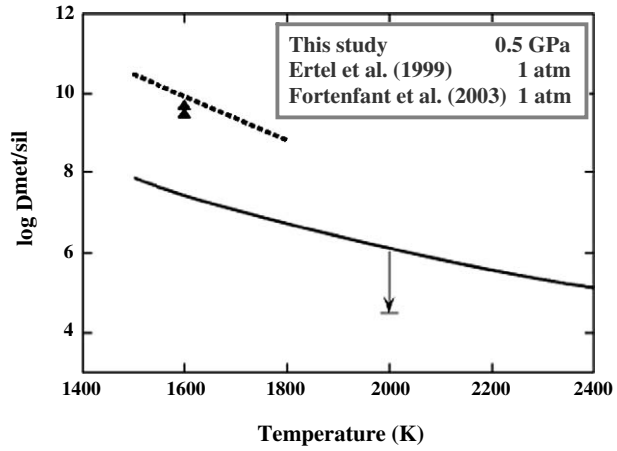

Fig. 7. Log $D^{met/sil}$ versus temperature (K) based on regression of the "average-lowest" data set to Eq. (2) (at IW + 1). The solid line shows values calculated at 0.5 GPa, and the vertical arrow shows values calculated from 0.5 to 40 GPa at 2000 K. The dashed line shows the parameterized temperature effect from the experiments of Fortenfant et al. (2003) at 1 atm recalculated at IW + 1 assuming divalent Pt. Black triangles correspond to the 1 atm results of Ertel et al. (1999) recalculated to IW + 1. All investigations shown were performed in identical bulk melt composition (1 atm AnDi eutectic melt).

given temperature when calculated to the same fO_2 (assuming divalent Pt in the silicate) in the 1 atm data. Although only speculation at this point, a potential explanation might be a significant difference in the melt structure and/or the coordination of Pt between the 1 atm liquid and the compressed AnDi melt, as has been reported for Ni and Co (Keppler and Rubie, 1993).

Holzheid et al. (2000) also investigated Pt partitioning at high pressures and temperatures, and recalculated their raw data to conditions of 1773 K and IW − 2.3 (see their Table 1). We calculated $D^{met/sil}$ at the same conditions, and the results are shown on Fig. 8. While the data of Holzheid et al. (2000) show too much scatter to reveal any pressure effect, we note that our model values generally fall within the range of the Holzheid et al. (2000) data. The general agreement between studies suggests that melt composition is not an important parameter, as Holzheid et al. (2000) used considerably different starting compositions. Indeed, melt compositions among experiments ranged dramatically from An-Di eutectic and MgO-rich basaltic composition at 1 atm to low melting K_2O–Na_2O–FeO composition above 2 GPa.

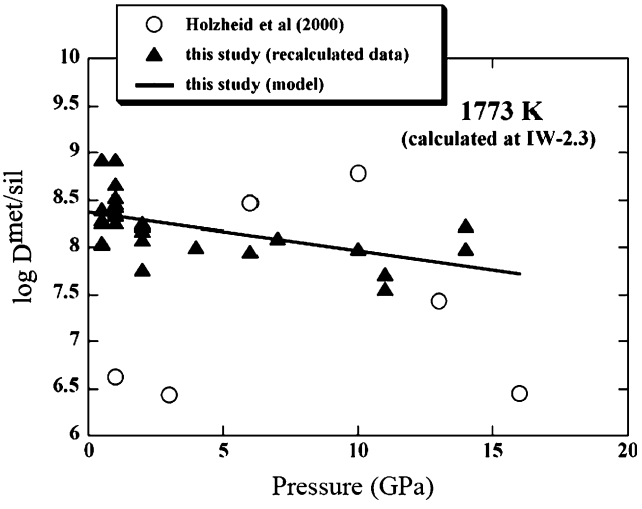

Fig. 8. Log $D^{met/sil}$ for Pt at infinite dilution in liquid Fe as a function of pressure (GPa) at IW − 2.3 and 1773 K. Open circles are recalculated data from Holzheid et al. (2000) (see their Table 1). The solid line is calculated from our model regressions to the "average-lowest" data assuming $\gamma(Pt) = 1$ (see Table 2).

5. Discussion

Recent magma ocean scenarios for metal/silicate equilibrium based on modeling of moderately siderophile elements like Ni, Co, and W indicate much higher temperature and pressure conditions for core-mantle equilibration than reached in our experiments (e.g., Li and Agee, 1996; Righter and Drake, 1997; Walter et al., 2000; Gessmann and Rubie, 1998, 2000; Li and Agee, 2001; Chabot and Agee, 2001, 2002, 2003; Wade and Wood, 2005). Here, we have used the regression to the average-lowest data set to estimate $D^{met/sil}$ at conditions appropriate for a deep magma ocean.

We are forced to make several assumptions in our approach to modeling core formation in Earth.

1. Core segregation from the mantle in the proto-Earth was an equilibrium process starting from a bulk chondritic protolith.
2. Moderately siderophile elements give a strong signal that core and mantle materials largely equilibrated within a range of pressure and temperature of about 20 to 60 GPa and in the range of 2000–4000 K, conditions that are at higher pressures and temperatures than reached in our experiments. Thus, to test these conditions we must assume our regressions provide an accurate means for extrapolation of pressure and temperature effects on partitioning. The validity of this assumption awaits further high P–T experimentation, and we reiterate that extrapolations of regressed data must always be viewed with caution.
3. We assume Pt is stable as a divalent species in silicate melt (PtO).
4. We do not know a priori the prevalent oxygen fugacity during core-mantle equilibrium. Based on the amount of FeO in modern primitive mantle (~8 wt%), a value of approximately ~IW − 2 is strongly implicated. For a divalent cation, a one log unit decrease in fO_2, for example from IW + 1 to IW, increases log $D^{met/sil}$ by 0.5 units. We model a range of oxygen fugacities from IW to IW − 2.
5. Above, we calculated $D^{met/sil}$ for Pt as the inverse of Pt solubility. This is only correct if Pt mixes ideally in molten metallic iron and silicate melt. Assuming Henrian behavior for the activity of PtO in silicate melt, then

$$D^{\mathrm{met/sil}} = 1/[\gamma(\mathrm{Pt}) \cdot X_{\mathrm{sil}}(\mathrm{PtO})], \quad (3)$$

where γ(Pt) is the activity of Pt in molten iron and X_{sil}(PtO) is the concentration of Pt in the silicate melt at its solubility limit (see Borisov and Palme, 1994b; O'Neill et al., 1995). We have determined X_{sil}(PtO) in our experiments, so it is γ(Pt) that we need to know to calculate a $D^{met/sil}$ appropriate for modeling core formation in Earth. γ(Pt) at infinite dilution in molten iron is not known at the conditions of our experiments. At low pressures (1 atm to 2 GPa) and at temperatures below the iron melting point, γ(Pt) is of the order 10^{-3} at infinite dilution in solid iron (Gudmundsson and Holloway, 1993; Kessel et al., 2001). Here, we take two modeling approaches to gauge the effect of γ(Pt). In one, we assume ideal mixing where $\gamma(\mathrm{Pt}) = 1$, in the other, we assume $\gamma(\mathrm{Pt}) = 10^{-3}$.

6. We assume silicate melt composition has no effect on Pt partitioning.

Here, we test whether $D^{met/sil}$ for Pt can conceivably approach the required low value of ~1000 to account for its abundance in the mantle at magma ocean conditions. We calculate $D^{met/sil}$ over a wide range of pressures, temperatures and oxygen fugacities. Fig. 9 shows that higher pressure, higher temperature, higher oxygen fugacity, and higher γ(Pt) all conspire to reduce $D^{met/sil}$. Fig. 9a shows that when γ(Pt) is assumed to be one, then for an estimated fO_2 of near IW, $D^{met/sil}$ can reach ~1000 at conditions of about 40 GPa and 4000 K. We find it very unlikely that neither Pt mixes ideally in molten iron at high pressure and temperature nor the oxygen fugacity prevalent in the mantle during core segregation was so high, as this would leave >20 wt% FeO in the mantle. Again, modeling of moderately siderophile element abundances in the mantle are consistent with a prevailing fO_2 in the region of IW − 2 (e.g., Wade and Wood, 2005).

Fig. 9b shows that even at the most extreme conditions of high-pressure, -temperature, and -oxygen fugacity considered $D^{met/sil}$ for Pt is several orders of magnitude too high to account for metal silicate equilibrium in Earth if γ(Pt) is ~10^{-3}. Based on these models we find it highly unlikely that Pt abundances in the mantle could have been established by core-mantle equilibration, a conclusion shared by Holzheid et al. (2000) and Fortenfant et al. (2003). Our models show that for the modern 'consensus' conditions for metal-silicate equilibrium in a deep magma ocean (e.g., somewhere in the range of 30–50 GPa, 2500–3500 K, IW − 1.5 to IW − 2.5), the $D^{met/sil}$ value for Pt would be more than 2 orders of magnitude too great to account for the mantle budget.

6. Conclusions

We have measured the solubility of Pt in anorthite-diopside eutectic melt from 0.5 to 14 GPa and 1723–2223 K. We have concluded that nanonuggets are part of the stable metal phase and that average-lowest analyses yield meaningful solubility limits. Parameterizations of $D^{met/sil}$ show that increasing pressure, and to a greater extent increasing temperature, make Pt more lithophile. Modeling of core formation within the context of the magma ocean model indicates that it is highly unlikely that the abundance of Pt in the mantle was established by core-mantle equilibration. This result does depend, however, on proper accounting of activity–composition relationships and the future confirmation of the extrapolation of pressure and temperature effects on partitioning predicted by the parameterizations.

The high-pressure and -temperature partitioning behavior of other HSE is generally not know. However, given their vastly differing low temperature geochemical behavior, a common metal/silicate partitioning coefficient for all HSE at high P–T conditions—necessary for the establishment of a chondritic element ratio in the upper mantle—stretches credulity. Based on the present data set for Pt, it seems much more likely that upper mantle abundances of HSE were established by the late addition of chondritic material after core formation had effectively

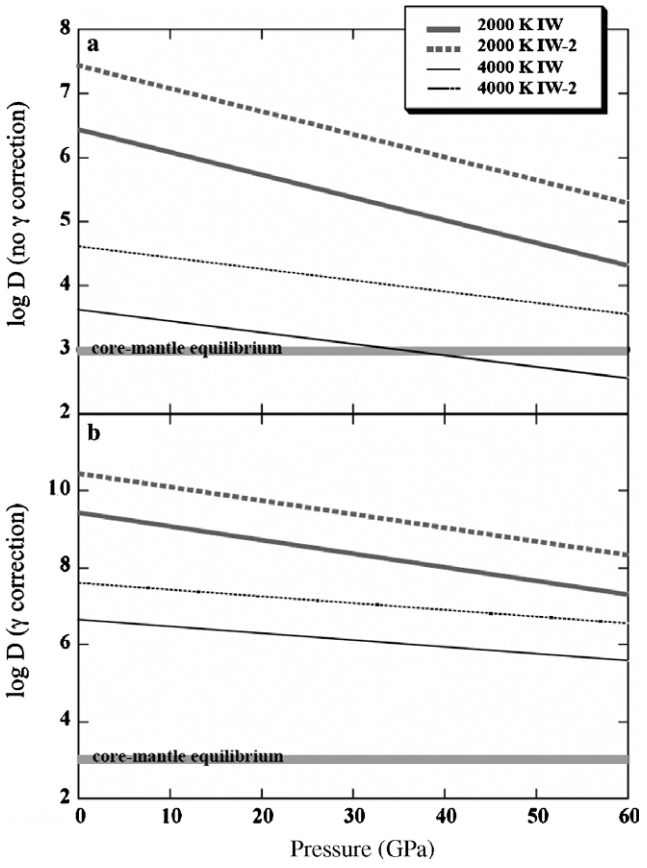

Fig. 9. Log $D^{met/sil}$ for Pt as a function of pressure, temperature and oxygen fugacity based on regression of Eq. (2) using "average-lowest" data set (Table 2). Log $D^{met/sil}$ is shown at IW and IW − 2 (solid and dashed lines, respectively) and at 2000 and 4000 K (thin and thick lines, respectively). Fig. 9a shows model log $D^{met/sil}$ assuming $\gamma(\mathrm{Pt}) = 1$. Fig. 9b shows model log $D^{met/sil}$ assuming $\gamma(\mathrm{Pt}) = 10^{-3}$. The value of log $D^{met/sil}$ for core-mantle equilibrium is ~3.

ceased. This material may have been added in the form of a 'veneer' of small objects, or perhaps as a one-off event involving a larger (but still small) impactor. This elegantly explains both the near chondritic relative element ratios of all HSE, and the nearly chondritic Re/Os ratio (to within 7%) in the primitive upper mantle. Late addition of HSE in chondritic element ratios to a vigorously convecting magma ocean after core formation had isolated metal from the magma ocean would have been a very effective way to mix them into the upper mantle.

Acknowledgments

The present study was funded by NSF Grant EAR0074036, NASA Grant NAG5-9435, and NASA Grant NAG5-12795 to Prof. Michael J. Drake. Many thanks to Prof. Eiji Ito for access to the high pressure facility at the Institute for Study of the Earth's Interior (Okayama University, Misasa, Japan), where all MA experiments were carried out. Mike Turbrett is thanked for his help and support during LA-ICPMS analyses. Memorial University's ICPMS facility is supported by an NSERC Major Facilities Access award. Many thanks as well to Ken Domanik from LPL for his support and assistance during performed EMP analyses.

Associate editor: F.J. Ryerson

References

Ballhaus, C., Sylvester, P.J., 2000. Noble metal enrichment processes in the Merensky Reef, Bushveld complex. *J. Petrol.* **41**, 545–561.

Borisov, A., Palme, H., 1994a. The solubility of palladium in silicate melts: implications for core formation in the Earth. *Geochim. Cosmochim. Acta* **58**, 705–716.

Borisov, A., Palme, H., 1994b. Solubilities of highly siderophile elements in silicate melts: experimental results and geochemical implications. *LPSC Contrib.* **921**, 33.

Borisov, A., Palme, H., 1994c. The solubility of Pt in silicate melts: experiments under oxidizing conditions. *LPSC* **25**, 141–142.

Borisov, A., Palme, H., 1995. The solubility of iridium in silicate melts: new data from experiments with $Ir_{10}Pt_{90}$ alloys. *Geochim. Cosmochim. Acta* **59**, 481–485.

Borisov, A., Palme, H., 1997. Experimental determination of the solubility of Pt in silicate melts. *Geochim. Cosmochim. Acta* **61**, 4349–4357.

Borisov, A., Palme, H., 1998. Experimental determination of Os metal/silicate partitioning. *N. Jb. Mineral. Abh.* **172**, 347–356.

Borisov, A., Lindstrom, D.J., Jones, J.H., 1999. An experimental study of Re solubility in Silicate Melts. *EOS suppl.* **80**, No 17, V32C-08, 365.

Chabot, N.L., Agee, C.B., 2001. The effect of core-mantle differentiation on V, Cr, and Mn: Experimental metal/silicate partitioning results. *LPSC XXXII*, abstract # 1686, Houston.

Chabot, N.L., Agee, C.B., 2002. The behavior of nickel and cobalt during core formation. *LPSC* **XXXIII**; abstract #1009, Houston.

Chabot, N.L., Agee, C.B., 2003. Core formation in the Earth and Moon: new experimental constraints from V, Cr, and Mn. *Geochim. Cosmochim. Acta* **67**, 2077–2091.

Cottrell, E.A., Walker, D., 2002. A new look at Pt solubility in silicate liquid. *LPSC* **XXXIII**, abstract #1274, Houston, 2002.

Dingwell, D.B., O'Neill, H.St.C., Ertel, W., Spettel, B., 1994. The solubility and oxidation state of Ni in silicate melt at low oxygen fugacities: results using a mechanically assisted equilibration technique. *Geochim. Cosmochim. Acta* **58**, 1967–1974.

Ertel, W., 1996. Bestimmung des Löslichkeitsverhaltens und der Metal-Silikat-Verteilungs-koeffi-zienten der siderophilen Elemente (Ni, W, Ir, Pt, Rh und Re) in einer haplobasaltischen Schmelze bei hohen Temperaturen. Ph.D. Thesis, 154 pages, BGI, University of Bayreuth.

Ertel, W., O'Neill, H.St.C., Sylvester, P.J., Dingwell, D.B., 1999. Solubilities of Pt and Rh in a haplobasaltic silicate melt at 1300 °C. *Geochim. Cosmochim. Acta* **63**, 2439–2449.

Ertel, W., O'Neill, H.St.C., Sylvester, P.J., Dingwell, D.B., Spettel, B., 2001. The solubility of rhenium in silicate melts: implications for the geochemical properties of rhenium at high temperatures. *Geochim. Cosmochim. Acta* **65**, 2161–2170.

Fortenfant, S.S., Günther, D., Dingwell, D.B., Rubie, D.C., 2003. Temperature dependence of Pt and Rh solubilities in a haplobasaltic melt. *Geochim. Cosmochim. Acta* **67**, 123–131.

French, B.M., 1966. Some geological implications of equilibrium between graphite and a C-H-O gas phase at high temperatures and pressures. *R. Geophys.* **4**, 223–253.

French, B.M., Eugster, H.P., 1965. Experimental control of oxygen fugacities by graphite–gas equilibrium. *J. Geophys. Res.* **70**, 1529–1539.

Gessmann, C.K., Rubie, D.C., 1998. The effect of temperature on the partitioning of nickel, cobalt, manganese, chromium, and vanadium at 9 GPa and constraints on formation of the earth's core. *Geochim. Cosmochim. Acta* **62**, 867–882.

Gessmann, C.K., Rubie, D.C., 2000. The origin of the depletions of V, Cr, and Mn in the mantles of the earth and Moon. *Earth Planet. Sci. Lett.* **184**, 95–107.

Gudmundsson, G., Holloway, J.R., 1993. Activity–composition relationships in the system Fe-Pt at 1300 and 1400 °C and at 1 bar and 20 kbar. *Am. Miner.* **78**, 178–186.

Hillgren, V., 1991. Partition behavior of Ni, Co, Mo, and W between basaltic liquid and Ni-rich metal: implications for the origin of the moon and lunar core formation. *Geophys. Res. Lett.* **18**, 2077–2080.

Holzheid, A., Grove, T.L., 2002. Sulfide saturation limits in silicate melts and their implication to core formation scenarios for terrestrial planets. *Am. Miner.* **87**, 227–237.

Holzheid, A., Sylvester, P.J., O'Neill, H.St.C., Rubie, D.C., Palme, H., 2000. Evidence for a late chondritic veneer in the Earth's mantle from high-pressure partitioning of palladium and Pt. *Nature* **406**, 396–399.

Kavner, A., Jeanloz, R., 1998. High-pressure melting curve of platinum. *J. Appl. Phys.* **83**, 7553–7559.

Keppler, H., Rubie, D.C., 1993. Pressure-induced coordination changes of transition-metal ions in silicate melts. *Nature* **364**, 54–56.

Kessel, R., Beckett, J.R., Stolper, E.M., 2001. Thermodynamic properties of the Pt–Fe system. *Am. Miner.* **86**, 1003–1014.

Kimura, K., Lewis, R.S., Anders, E., 1974. Distribution of gold and rhenium between nickel- iron and silicate melts: implications for the abundance of siderophile elements on the Earth and Moon. *Geochim. Cosmochim. Acta* **38**, 683–701.

Li, J., Agee, C., 1996. Geochemistry of mantle-core formation at high pressure. *Nature* **381**, 686–689.

Li, J., Agee, C.B., 2001. The effect of pressure, temperature, oxygen fugacity and composition on partitioning of nickel and cobalt between liquid Fe-Ni-S alloy and liquid silicate: implications for the Earth's core formation. *Geochim. Cosmochim. Acta* **65** (11), 1821–1832.

McDonough, W.F., Sun, S.-S., 1995. The Composition of the Earth. *Chem. Geol.* **120**, 223–253.

Newsom, H.E., 1990. Accretion and core formation in the Earth: evidence from siderophile elements. In: Newsom, H.E., Jones, J.H. (Eds.), *Origin of the Earth*. Oxford Univ. Press, New York, pp. 273–288.

Newsom, H.E., Sims, K.W.W., Noll Jr., P.D., Jaeger, W.L., Maehr, S.A., Beserra, T.B., 1996. The abundance of W in the bulk silicate Earth: constraints on core formation. *Geochim. Cosmochim. Acta* **60**, 1155–1169.

O'Neill, H.St.C., 1991a. The origin of the Moon and the early history of the earth—a chemical model Part1: the Moon. *Geochim. Cosmochim. Acta* **55**, 1135–1157.

O'Neill, H.St.C., 1991b. The origin of the Moon and the early history of the earth—a chemical model. Part 2: The Earth. *Geochim. Cosmochim. Acta* **55**, 1159–1172.

O'Neill, H.St.C., Palme, H., 1998. Composition of the silicate Earth: implications for accretion and core formation. In: Jackson, I. (Ed.), *The Earth's Mantle, Composition, Structure and Evolution*. Cambridge Univ. Press, Cambridge, pp. 3–136.

O'Neill, H.St.C., Dingwell, D.B., Borisov, A., Spettel, B., Palme, H., 1995. Experimental petrochemistry of some highly siderophile elements at high temperatures, and some implications for core formation and the mantle's early history. *Chem. Geol.* **120**, 255–273.

Pouchou, J.L., Pichoir, F., 1984. A new model for quantitative x-ray microanalysis—Part 1: application to the analysis of homogeneous samples. *Res. Aerospat.* **3**, 13–38.

Presnall, D.C., Dixon, S.A., Dixon, J.R., O'Donnell, T.H., Brenner, N.L., Schrock, R.L., Dycus, D.W., 1978. Liquidus phase relations on the join Diopside-Forsterite-Anorthite from 1 bar to 20 kbar: their bearing on the generation and crystallization of basaltic magma. *Contrib. Min. Petrol.* **66**, 203–220.

Righter, K., Drake, M.J., 1997. Metal-silicate equilibrium in a homogeneously accreting earth: new results for Re. *Earth Planet. Sci. Lett.* **146**, 541–553.

Righter, K., Drake, M.J., Yaxley, G., 1997. Prediction of siderophile element metal-silicate partition coefficients to 20 GPa and 2800 °C: the effects of pressure, temperature, oxygen fugacity, and silicate and metallic melt compositions. *Phys. Earth Planet. Inter.* **100**, 115–134.

Ringwood, A.E., 1984. The Earth's core: its composition, formation and bearing upon the origin of the Earth. *Proc. R. Soc. Lond. A* **395**, 1–46.

Strong, H.M., Bundy, F.P., 1959. Fusion curves of 4 group-VIII metals to 100,000 atmospheres. *Phys. Res.* **115**, 278–284.

Sylvester, P.J., Eggins, S.M., 1997. Analysis of Re, Au, Pd, Pt and Rh in NIST glass certified reference materials and natural basalt glasses by laser-ablation ICP-MS. *Geostandards Newslett.* **21**, 215–228.

Van Achterbergh, E., Ryan, C.G., Jackson, S.E., Griffin, W.L., 2001. Data reduction software for LA-ICP-MS. In: Sylvester, P. (Ed.), Laser Ablation-ICPMS in the Earth Sciences, Principles and Applications, MAC Short Course Volume 29, pp. 239–243.

Wade, J., Wood, B., 2005. Core formation and the oxidation state of the Earth. *Earth Planet. Sci. Lett.* **236**, 78–95.

Wänke, H., 1981. Constitution of terrestrial planets. *Philos. Trans. R. Soc. Lond.* **303**, 287–302.

Wänke, H., Dreibus, G., Jagoutz, E., 1984. Mantle chemistry and accretion history of the Earth. In: Kröner, A. et al. (Eds.), *Archean Geochemistry: The Origin and Evolution of the Archean Continental Crust*. Springer-Verlag, Berlin, pp. 1–24.

Walter, M.J., Thibault, Y., Wei, K., Luth, R.W., 1995. Characterizing experimental pressure and temperature conditions in multi-anvil apparatus. *Can. J. Phys.* **73**, 273–286.

Walter, M.J., Newsom, H.E., Ertel, W., Holzheid, A., 2000. Siderophile elements in the Earth and Moon. Metal/silicate partitioning and implication for core formation. In: Canup, R.M., Righter, K. (Eds.), *Origin of the Earth and Moon*. University of Arizona Press, Tucson, AZ, pp. 265–289.

Wendlandt, R.F., 1982. Sulfide saturation of basalt and andesite melts at high pressures and temperatures. *Am. Miner.* **67**, 877–885.